



Formation mechanism of AlNbTiVZr high entropy alloy/Ti multi-principal element alloy by laser direct energy deposition: Microstructure evaluation and mechanical properties

Yumeng Zhang, Yiqing Zhao, Longxiang Sun, Leilei Wang, Linqin Li, Xiaohong Zhan*

College of Materials Science and Technology, Nanjing University of Aeronautics and Astronautics, Nanjing 211106, China



ARTICLE INFO

Keywords:

High-entropy alloy
Microstructure
Mechanical properties
Fracture toughness

ABSTRACT

A novel refractory multi-principal element alloy with high strength and toughness matching characteristics was successfully prepared by mixing TA15 alloy with AlNbTiVZr high-entropy alloy. The effects of the composition ratio of the high-entropy alloy on the microstructure evolution and its influence on properties were investigated in this study. The tensile strength of the 70 wt % AlNbTiVZr HEA/Ti multi-principal element alloy is 1.18 times more than that of TA15 alloy, which has a value of 1068.0 ± 2.1 MPa. The increase in strength is mainly due to the production of equiaxed fine grains and the development of a robust and resilient body-centered cubic (BCC) phase in the alloy following the introduction of the high-entropy alloy. The attainment of the acceptable tensile strain is the result of the combined influence of the BCC matrix phase and the dispersed second-phase particles. The exceptional mechanical capabilities of the 70 wt % AlNbTiVZr/Ti multi-principal element alloy undeniably enhance its potential for use as a structural component in aerospace load-bearing constructions.

1. Introduction

Titanium and titanium-based alloys, such as commercially pure titanium and TA15, have found extensive application in the aerospace industry owing to their exceptional blend of strength, toughness, ductility, and resistance to corrosion [1–4]. Nevertheless, pure titanium generally exhibits a relatively low tensile yield strength, approximately measuring at 600 MPa [5,6]. Titanium matrix composites [7–9] hold great potential for widespread use in the automotive and aerospace industries, as well as other industrial applications. The utilisation of additive manufacturing processes in the production of these composite components, which are based on titanium, provides notable benefits. Due to the difficulties and expenses associated with adding reinforcements to the wire, a more convenient approach is to enhance them by blending particles into titanium alloy powders. This is particularly advantageous when employing the direct energy deposition method with lasers. Laser-directed energy deposition (L-DED) technique enables the direct feeding of powder to the deposition site [10–13]. This powder is rapidly melted by a high-energy density laser beam, resulting in the formation of the deposition layer. When compared to other methods of additive manufacturing, LDED has a better level of production efficiency and is well-suited for making large components.

Additionally, it provides the flexibility to freely modify the composition of the powder used. Scholars have recommended particle reinforcement and fiber reinforcement as typical approaches to enhance the mechanical properties of titanium matrix composites. Particle reinforcement, in comparison to fiber reinforcement, possesses the qualities of material homogeneity, various synthesis methods, and easily accessible processing technology. It exploits the interaction between cracks and high-strength second-phase particles, thereby enhancing the activation energy required for crack propagation. The crack propagation path was modified, leading to a change in the mechanical failure mode of the matrix. As a result, the mechanical characteristics of the titanium alloy were enhanced [14–16]. Yifeng Xiong et al. [17] utilized Ti_3AlC_2 ceramic particles to reinforce the Ti-6.5Al-2Zr-1Mo-1 V (TA15) alloy. They created a composite material with a network structure by employing low energy ball milling (LEBM) and spark plasma sintering processes. In the three-dimensional network architecture, the reinforcing layer is distributed around the interface of the TA15 matrix. The hardness, tensile strength, and compressive strength of the Ti_3AlC_2 -TiC/TA15 composite material are significantly improved, with little loss of ductility. Faming Zhang et al. [18] synthesized in-situ Ti_2AlC ceramic phase in the TA15 matrix to improve the mechanical properties of the TA15 alloy by utilizing its higher strength. The addition of 1.0 wt %

* Corresponding author.

E-mail address: xiaohongzhan_nuua@126.com (X. Zhan).

Ti_2AlC ceramic phase resulted in minimal sacrifice in ductility for the TA15 alloy. Qi Zhang [19] et al. incorporated TiB_2 whiskers into the TC4 matrix to prepare a composite material with higher strength. Testing showed that the strength increased by 50 wt % compared to pure TC4, while the ductility decreased by approximately 60 wt %. Yangju Feng [20] et al. added 2.5 wt % TiB_2 particles into the TA15 matrix to fabricate a novel columnar network-reinforced $\text{TiBw}/\text{TA15}$ composite material with excellent strength and high plasticity. Test results indicated a 25 wt % increase in strength while the ductility was only 7.1 wt % of the previous level. Shuai Wang et al. [21] added TiB_2 with a content of 1 wt % to 2.5 wt % to TA15 alloy, leading to the in-situ formation of a network-like TiB phase at grain boundaries. This increased the tensile strength of titanium matrix composite by approximately 20 wt %, with a reduction in plasticity of about 15 wt %.

Compared with ceramic particles, high entropy alloys have high strength and good plasticity, and the coefficient of thermal expansion between high entropy alloys and the matrix is similar. Zhanwei Yuan et al. [22] added 7 wt % $\text{CoCrFeNiMo}_{0.2}$ HEA particles to pure titanium, and the diffusion layer formed at the interface enhanced the bonding ability between the particles and the matrix, which resulted in the successful fabrication of titanium-based composite with higher strength. Fei Qiang et al. [23] added 10 wt % $\text{Al}_{0.6}\text{CoCrFeNi}$ to pure titanium, producing titanium-based composite materials reinforced with high-entropy alloy particles. The limited diffusion layer formed between the HEA layer and the matrix led to the formation of strengthened second phases in the surrounding matrix, ultimately enhancing the mechanical properties of pure titanium. Tao Xiang et al. [24] discovered that adding 60 wt % TiZrNbTa high-entropy alloy (HEA) particles to a titanium matrix achieved a balance between strength and ductility by establishing a bimodal grain size distribution (BGSD) that induced the ultra-high strength TiZrNbTa HEA with nanoscale grain size into the coarse-grained pure titanium. When the elements in the reinforcement undergo solid solution diffusion in the matrix, the performance of the matrix can be further enhanced. Therefore, if a material with strengthening elements similar to the matrix's melting point is used as the reinforcement, allowing for full fusion in the liquid state, a different strengthening effect will be achieved.

It is well known that different elements have different effects on the properties of titanium alloys [25–27]. The importance of solid solution strengthening lies in augmenting the mechanical characteristics of materials, specifically in elevating their strength and hardness. This process can be accomplished by alloying or incorporating additional elements, hence enhancing the performance of the material. The objective of investigating this innovative composite material is to discover material solutions that offer superior performance and greater sustainability, in order to fulfil the increasing engineering demands and environmental standards. The addition of alloying elements to the alloy has a substantial influence on the type of strengthening that occurs in the alloy. Elements with smaller atomic radii, such as B, C and N, result in interstitial strengthening. On the other hand, elements with larger atomic radii, such as Al, Mo, Nb, and Ti, form substitutional solid solutions [28–30]. For example, the addition of Nb and V can form solid solution strengthening, effectively improving mechanical properties. The presence of Mo can also enhance strength by forming dispersed precipitates. These elements can hinder the movement of dislocations, increasing the alloy's yield strength. Additionally, alloying elements can improve the hardness of TA15 alloy. The formation of solid solution and the presence of precipitates can increase the alloy's hardness, making it more resistant to deformation and wear. Furthermore, alloying elements can improve the ductility and toughness of TA15 alloy. The addition of Ti can refine the grain structure and improve the alloy's resistance to cracking. This can enhance ductility and toughness, making the alloy more suitable for applications requiring high impact resistance. Based on these ideas, researchers have proposed multi-element alloying as a method to strengthen titanium alloys. Jinlong Su et al. [31] prepared multi-element composites by adding CoCrNi high-entropy alloy to TC4

titanium alloy. The diffusion of Co, Cr, and Ni from the high-entropy alloy into the TC4 alloy promoted the decomposition of the α phase and increased the proportion of the β phase, resulting in a 10 % increase in the strength of the TC4 titanium alloy. Yingchun Fang et al. [32] added a multi-element Fe-Cr-Ni-Mo alloy in the form of 316 L steel to a titanium matrix, retaining the β phase in the TC4 alloy. This resulted in the $\text{Ti}-1.35\text{Fe}-0.36\text{Cr}-0.24\text{Ni}-0.05\text{Mo}$ alloy having a higher ultimate tensile strength (635 MPa) and greater uniform elongation (12 %). Therefore, multi-element alloying is also an effective method for strengthening titanium alloys. In order to fully utilize the high strength of high-entropy alloy (HEA) particles and the alloying effect after element diffusion, this study mixed a lightweight refractory high entropy alloy consisting of five elements (Al, Nb, Ti, V, Zr) with TA15 alloy. By taking advantage of their similar melting points, the HEA was fully melted in the matrix, forming a Ti-Al-V-Zr-Nb-Mo multi-element alloy system to enhance the mechanical properties of TA15 alloy.

According to previous studies, the high-entropy alloy $\text{Al}_{0.8}\text{Nb}_{0.5}\text{-Ti}_2\text{V}_2\text{Zr}_{0.5}$ demonstrates superior strength at both room temperature (about twice than that of Inconel 718) and high temperatures. However, its plasticity is somewhat limited. Thus, by immediately applying high-entropy alloy layers onto the surface of TA15 alloy, it is susceptible to the formation of deep cracks. A gradient layer can be formed by mixing the TA15 alloy with the high-entropy alloy [33]. This paper describes the preparation of HEA/Ti multi-principal element alloys through the mixing of high-entropy alloys with TA15 alloy, utilizing laser-directed energy deposition. The alloys are prepared by laser melting deposition. The effect of high entropy alloy content on the mechanical properties of multi-principal element alloy was researched, and the formation sequence of phases in multi-principal element alloys is discussed in detail.

2. Materials and experimental procedures

2.1. Materials

High entropy alloy AlNbTiVZr powder was prepared through the rotating electrode atomization in an argon shield with the raw materials (Al, Nb, Ti, V and Zr). The gas-atomized powders of the pure titanium with spherical shape and a size distribution ranging between 90 and 150 μm were used in this study. Fig. 1 displays the scanning electron microscope (SEM) morphology and particle size distribution of pure Ti powder and AlNbTiVZr powder. Table 1 presents the chemical composition (wt %) of AlNbTiVZr high entropy alloy powder. Before manufacturing, those powders were kept in vacuum at 102 °C, 8 h for drying. During the printing process, high-entropy alloy powder and TA15 powder are placed in two distinct powder barrels. The rotating speed of each barrel can be adjusted individually. The mass ratios of the HEA powder and mixed powder are 0:10, 2:8, 4:6 and 7:3. The obtained multi-principal element alloys are abbreviated as $x\text{-HEA}$, where x represents the percentage of HEA powder to the total powder mass.

2.2. LMD process

The LMD machine was equipped with the ytterbium fiber laser (wavelength of 1064 nm, beam diameter of 3 mm), powder and shield gas delivery, printing chamber, and computational control systems. The Laser melting deposition (LMD) process (Fig. 2a) used an RFL-C6000 laser machine to produce a 50 mm × 20 mm rectangular cuboid bulk on a TA15 plate ($\text{Ti}-6.5\text{Al}-2\text{Zr}-1\text{Mo}-1\text{V}$, wt %). A total of 12 layers of multi-track structure were deposited in an argon atmosphere, resulting in a final bulk height of 10 mm. The LMD parameters utilized 1600 W as laser power, 10 mm/s as scanning velocity. The Ar pressure was kept constant, and the oxygen concentration was kept less than 100 ppm to avoid oxidation during the LMD process. The bi-directional reciprocating scanning strategy with 50 % overlap ratio of multi-track was selected as a scanning path. Each vertex of the rectangular was chosen as

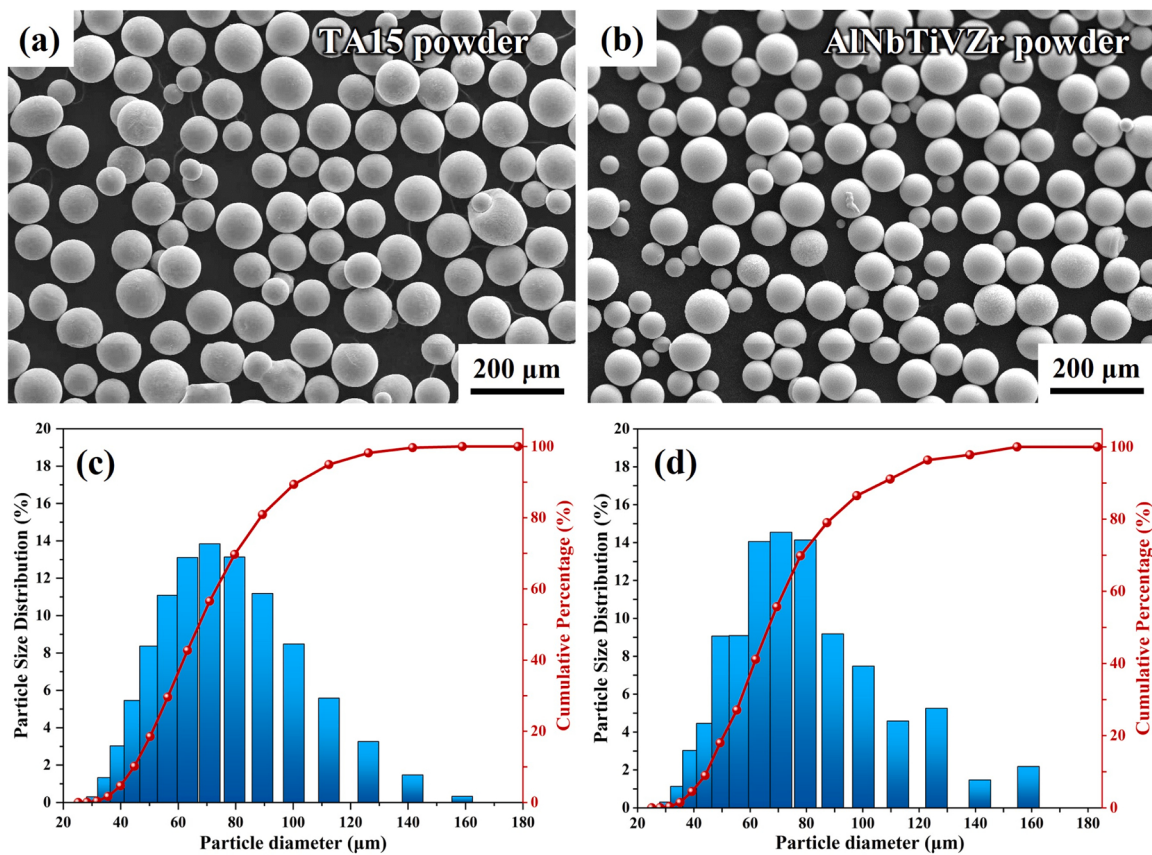


Fig. 1. SEM images of (a) the TA15 powder and $\text{Al}_{0.8}\text{Nb}_{0.5}\text{Ti}_2\text{V}_2\text{Zr}_{0.5}$ HEA powder prepared by plasma rotating electrode atomization and (b) the AlNbTiVZr powder prepared by gas atomization.

Table 1

Chemical composition of the TA15 and AlNbTiVZr powder (wt %).

Composition	Al	Zr	V	Mo	Nb	C	Fe	Ti
TA15	6.47	1.92	1.61	1.01	-	0.02	0.02	Bal.
AlNbTiVZr	6.9	14.67	32.75	-	14.92	-	-	30.76

the initial point. The volumetric energy density η is a useful metric to evaluate the influence of processing parameters. It is calculated as the following equation.

$$\eta = \frac{P}{\sqrt{vht}} = 160 \quad J/mm^3 \quad (1)$$

In this formula, P is the laser power, v is the scanning speed, h is the hatch space, and t is the layer thickness.

2.3. Microstructural observation and mechanical properties

All samples were imaged from the front view (YOZ section) to observe the microstructures. Wire electrical discharge machining (EDM) was used for all sample cutting. These specimens were polished by standard mechanical polishing procedures, and thus a final surface finish of $0.05 \mu\text{m}$ was obtained. Flat “dog-bone” tensile samples were cut along the horizontal direction, with gage sections of $6 \text{ mm} \times 40 \text{ mm} \times 2 \text{ mm}$. A Nexcope NM910-R digital microscope equipped with a Plan S-Apo wide-range zoom lens was used for optical imaging. Field-emission scanning electron microscopy (SEM, Zeiss SUPRA 55) was used to acquire the microstructures in the back-scattered electron (BSE) mode, with an operating voltage of 20 kV and a working distance of 10 mm. Electron backscatter diffraction (EBSD) was performed at 20 kV to identify the crystallographic orientation and phase compositions. The

step size ($0.5-1 \mu\text{m}$) of EBSD was chosen based on the sample features. The data were analyzed using AztecCrystal (Oxford). An XEmpyrean with Cu-K α diffraction was used to collect X-ray diffraction (XRD) patterns at 40 kV and 30 mA. The scan rate of the XRD device was $5^\circ/\text{min}$, the step size was 0.02° , and the 2θ diffraction angle was $5-87^\circ$. After that, tensile testing was conducted on an MTS test frame at a strain rate of $1 \times 10^{-3} \text{ s}^{-1}$ with an MTS extensometer directly attached to the gage section of the samples.

3. Results

3.1. Typical phases analysis

Fig. 3 displays the X-ray diffraction (XRD) pattern and scanning electron microscopy (SEM) image of a titanium alloy that has been doped with a high-entropy alloy, revealing its phase composition. The TA15 alloy consists mainly of the α -Ti phase with a minor presence of the β phase. The α -Ti phase has a spindle-shaped morphology, with a little presence of β phase localized at the extremities of the spindle-like structure. At a doping fraction of 20 wt %, the high-entropy alloy experiences an increase in aluminum content from 10.205 at % to 10.924 at %, and an increase in vanadium (V) content from 0 percent to 6.89 percent. The α phase undergoes a reduction in volume, leading to a gradual transformation from a spindle-shaped structure to a shorter rod-

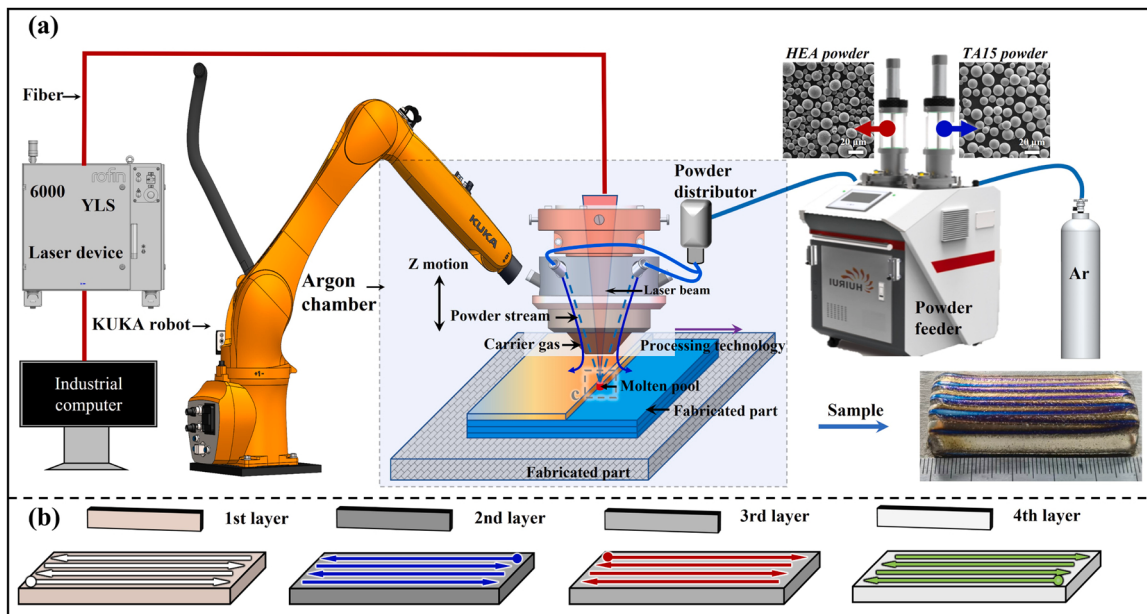


Fig. 2. Macroscopic photos of (a) schematic illustration of the equipment of LDED process and (b) the manufacturing method of the as-built complex alloys.

like one. Aluminum serves as a stabilizer for the α -Ti phase due to its atomic radius being 1.3 % lower than that of titanium (Ti). Introducing aluminum into the α -Ti phase results in a reduction in lattice constant of about 0.0064 %. The V and Nb elements undergo dissolution into the titanium lattice, resulting in the formation of a body-centered cubic (BCC) phase. The lattice deformation occurring between the body-centered cubic (BCC) phase and the α -Ti phase improves the strength of the multi-principal element alloys while diminishing its ductility. In the 70_HEA sample, there is a notable reduction in the content of the α -Ti phase, and the lattice constant reduces even further to 99.4 % of its initial value. Simultaneously, by introducing doping agents like Nb and V, the transformation temperature of the β phase falls, leading to a higher proportion of β phase being preserved as the dominant matrix phase, characterized by a typical body-centered cubic (BCC) structure. The BCC phase exhibits an increase in its composition, whereas the lattice constant experiences a drop of roughly 0.52 %. When the mass fraction of the high-entropy alloy in TA15 alloy surpasses 50 %, the proportion of the α -Ti phase diminishes to below 1 %. The BCC phase remains unchanged as the matrix phase without experiencing any phase transformation at room temperature. Presently, despite the V element content being below 20 %, the prevailing phase in the matrix is the Ti₄V phase.

Furthermore, the introduction of doping with the Nb element causes a displacement of the (110) BCC diffraction peak towards higher diffraction angles. The lattice parameters of the 0_HEA, 20_HEA, 40_HEA, and 70_HEA alloys were measured and found to be 3.321 Å, 3.316 Å, 3.312 Å, and 3.306 Å, respectively. The incorporation of vanadium (V) into titanium-based alloys has a notable impact on the crystal structure of the body-centered cubic (BCC) phase, as seen by the alterations in the BCC lattice. The diagram demonstrates that within the 20_HEA sample, α -Ti is still present within the β -Ti grains. The α -Ti phase, which has a hexagonal close-packed structure, exhibits a notable disparity in unit cell structure compared to the β phase. As a consequence, the microstructure experiences elevated solidification stress. However, the 70_HEA alloy exhibits a notable reduction in the amount of α -Ti phase, with the majority of grains consisting predominantly of the BCC phase. The interfacial stress between the α -Ti and BCC phases experiences a substantial reduction, resulting in a large decrease in solidification stress for both phases.

The primary component of a TA15 alloy is α -Ti, which is present in

the shape of elongated plate-like structures. Fig. 3b illustrates that adding 20 wt % of Al_{0.8}Nb_{0.5}Ti₂V₂Zr_{0.5} high-entropy alloy to TA15 alloy significantly decreases the volume of α -Ti phase. This causes a transformation from plate-like structures to shorter needle-like structures. The α -Ti phases, which have a similar appearance to short needle-like structures, coexist with small block-like BCC Laves phases. The C14 Laves phases are directly produced around the α -Ti phase and demonstrate a coherent relationship with it. By augmenting the proportion of the high-entropy alloy Al_{0.8}Nb_{0.5}Ti₂V₂Zr_{0.5} in the multi-principal element alloys to 70 percent, distributed C14 Laves phases (light gray) appear within the block-like matrix, while the α phase is almost eradicated. The C14 Laves phases, which exhibit a point-like structure, are distributed sporadically throughout the limits of the BCC phase. Based on the observation in Fig. 3d, it is clear that when the high-entropy alloy content approaches 70 wt %, the laves phases do not form a continuous network-like structure at the grain boundaries (white). Nevertheless, within the pristine high-entropy alloy, the C14 Laves phases congregate and create a cohesive network-like arrangement at the interfaces between grains, whereas the matrix consists of the body-centered cubic (BCC) phase [34].

3.2. Microstructure analysis

Fig. 4 displays noticeable alteration in the microstructure morphology of x_HEA ($x=0, 20, 40, 70$) as the proportion of enhanced phase particles increases. The TA15 alloy is classified as a columnar dendritic morphology. The addition of HEA noticeably increases the proportion of cellular grains and some nearly equiaxed grains in 20_HEA. The volume fraction of α -Ti phase decreases as a function of mass fraction of high entropy alloy.

Furthermore, the picture reveals a discernible color variation inside the grains of the 20_HEA and 70_HEA samples, suggesting the presence of distinct orientation angles within these grains. The regions where the densely packed hexagonal close-packed (HCP) phases (α -Ti and C14_Laves) and body-centered cubic (BCC) phases (β -Ti and Ti-Nb phases) are concentrated exhibit significant variations in grain orientation. This is due to the reduced radius of the Al atoms, which results in significant elastic constants and lattice distortion when combined with Zr atoms in the C14 Laves phase. Consequently, the C14 Laves phase exhibits characteristic brittleness. The number of slip systems in the BCC

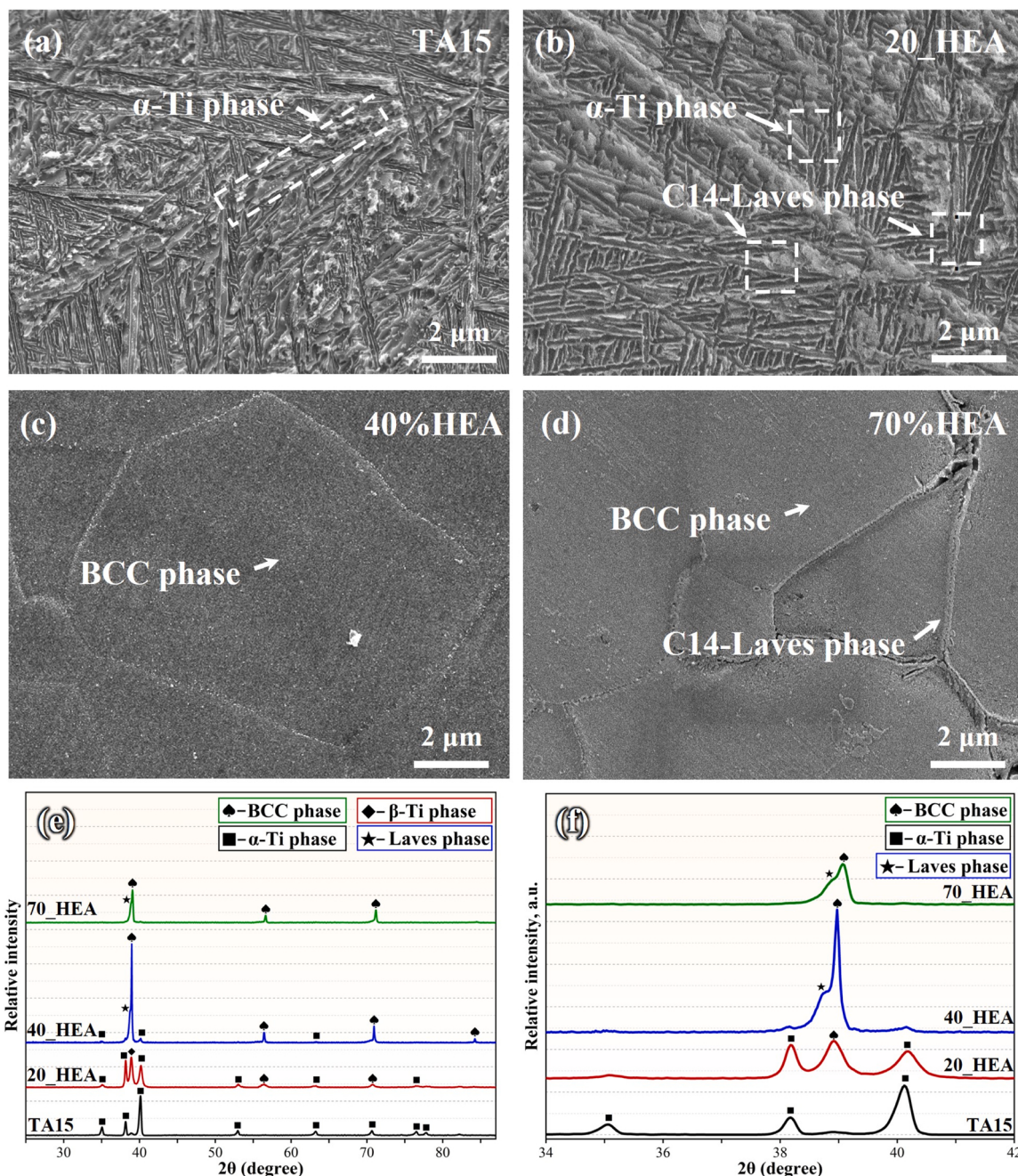


Fig. 3. SEM images of different titanium composites: (a) TA15 alloy, (b) 20_HEA, (c) 40_HEA, and (d) 70_HEA. (e) XRD patterns of LDED-produced HEA/Ti alloys, and (f) Enlarged diagram of XRD patterns in LDED-produced HEA/Ti alloys between 34° and 42° .

phase is greater than that in the C14 Laves phase. Throughout the development phase, the grains undergo compression from multiple directions in three-dimensional space. Grains that contain both of these phases may experience varying degrees of bending or protrusion, resulting in alterations in the orientation angles across different parts of the grains.

Fig. 5 depicts the alteration in grain orientation prior to and following the introduction of high-entropy alloy into the TA15 alloy. As shown in Fig. 5a, the TA15 alloy exhibits columnar grains and α phase, which align with the previously mentioned microstructure. Fig. 5b demonstrates that when doped with a 20 % high-entropy alloy, the deposited layers display the formation of C14 Laves phase. The C14 Laves phases are mostly localized at the interfaces between grains, leading to a reduction in the volume fraction of the α phase from 98 % to

3 %. These findings indicate that the presence of BCC-stabilizing elements like Nb and V in the high-entropy alloy strongly suppresses the formation of the α phase in the TA15 alloy. By raising the percentage of high-entropy alloy doping to 70 %, the α phase fraction is further decreased to 0.4 %, while the proportion of the BCC phase in the matrix is dramatically increased. Furthermore, the figure reveals a discernible color difference inside the grains in the deposition layers of 20 % HEA and 40 % HEA, suggesting the presence of varying orientation angles within these grains. The regions where the densely packed hexagonal close-packed (HCP) phases (α -Ti and C14 Laves) and body-centered cubic (BCC) phases (β -Ti and Ti-Nb phases) are concentrated exhibit distinct variations in grain orientation. The reason for this is that the aluminum (Al) atoms have a smaller atomic radius. When they combine with zirconium (Zr) atoms, the resulting C14 Laves phase exhibits

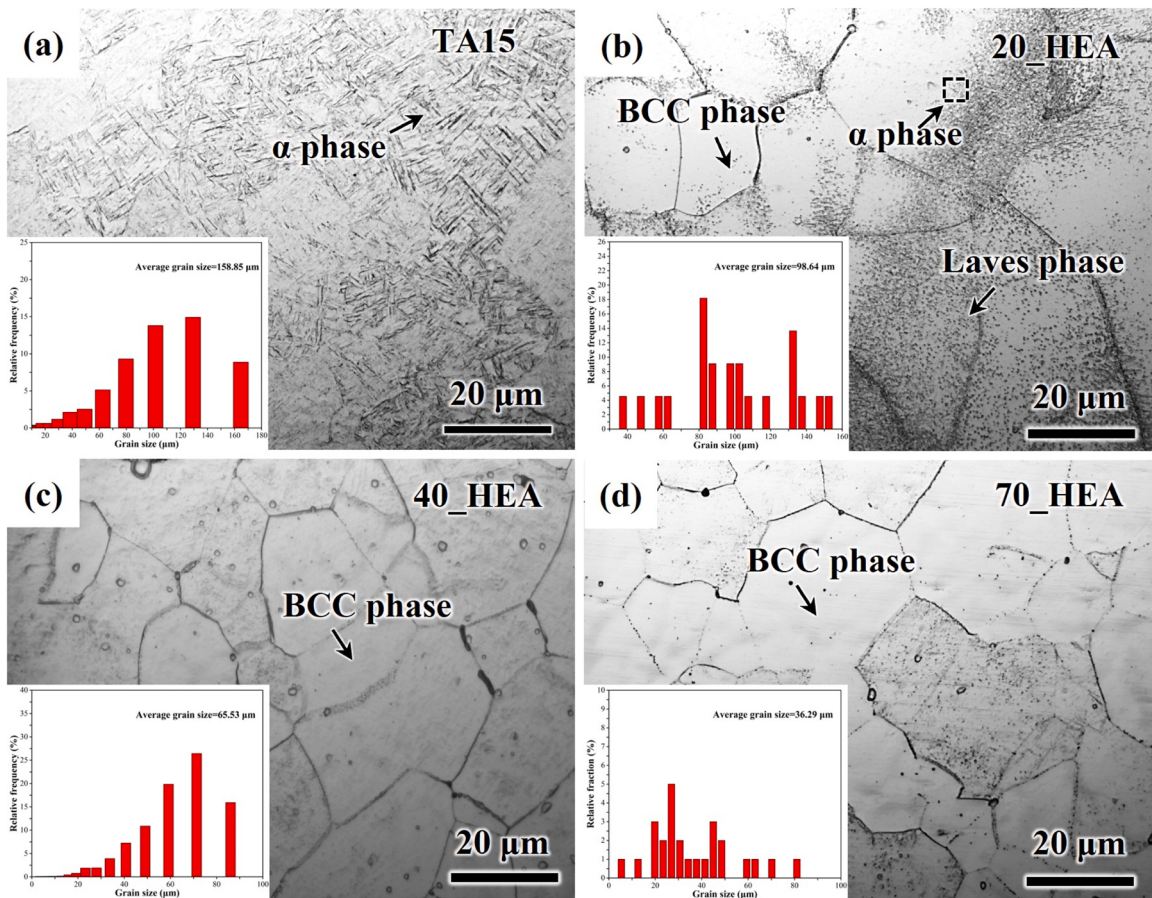


Fig. 4. Microstructure of titanium composite alloys with different mass fraction of high-entropy alloys.

significant elastic constants and lattice distortion. As a result, it becomes a typical brittle phase. In contrast, the body-centered cubic (BCC) phase has a greater number of slip systems compared to the C14 Laves phase. TA15 mostly comprises the hcp structure α phase. The grains experience internal deformation challenges caused by compressive forces from diverse directions during growth. This promotes the development of subgrains with varying orientations. Nevertheless, by incorporating the high-entropy alloy, the occurrence of the body-centered cubic (BCC) phase is enhanced, resulting in an augmented quantity of slip systems inside the grains. Consequently, this leads to a greater capacity for accommodating deformation. The diagram clearly illustrates a variation in the orientation of the grains, which is caused by the accommodative deformation.

3.3. Tensile strength and behaviors analysis

The strength and toughness of pure AlNbTiVZr high-entropy alloys exhibit a trade-off between these two qualities. When the Al component in the alloy is less than 10 %, it retains an elongation percentage of 20 % or higher, but the total strength remains relatively weak. Nevertheless, when the Al concentration in the high-entropy alloy surpasses 20 %, the strength of the alloy significantly rises to 1100 MPa, while the plasticity experiences a sudden decline to a range of 6–8 % [35]. By introducing high-entropy alloy into the TA15 alloy, the multi-principal-element alloys achieve a tensile strength of 1.1 GPa, surpassing the majority of additive TA15 alloys. The coupling of high-entropy alloys with titanium alloys in terms of strength and toughness offers substantial benefits. The Fig. 6a and b, display the engineering stress-strain, and strain hardening rate of the titanium composite samples that have been increased with multiple elements alloying. The TA15 alloy exhibit an ultimate tensile

strength (UTS) of up to 1068 MPa, as well as 85 % yield strength ranging from 880 to 910 MPa, and an elastic modulus varying from 80 to 90 GPa. In 20_HEA, the ultimate tensile strength (UTS) was raised to 1125 MPa, while the elongation decreased to 1.64 %. In 70_HEA, the strength dilated by 180 MPa and the strain was improved by 40 % compared to that of the 20_HEA samples. In addition, more pronounced decreases in the value of ultimate tensile strength below 700 MPa were observed in the high-entropy Al_{0.8}Nb_{0.5}Ti₂V₂Zr_{0.5} alloy samples. Correspondingly, the tensile strains also presented an obvious reduction. Among all the samples, the multilayered high-entropy alloys showed the minimum strain values of 5.64 %.

Fig. 7 illustrates the surface properties of a notched sample that underwent tensile tests, using different proportions of high-entropy alloy. The fracture of the TA15 alloy samples under tension exhibits a combination of features characteristic of both ductile and brittle fractures. The fracture surface exhibits distorted grains and slip characteristics. Compared with TA15 alloy samples, the high-entropy alloy exhibits distinct microcrack patterns and a network-like Laves phase at the interfaces between grains, with no discernible deformation occurring within the grains [36]. Thus, the addition of high-entropy alloy into TA15 alloy leads to substantial alterations in the fracture mode of the specimens. The addition of a high-entropy alloy with a weight percentage of 20 results in the formation of C14 Laves phases, which can be observed both at the borders and within the grains. Multiple slip bands, oriented at an angle of roughly 45° relative to the direction of tension, can be visible in the TA15 alloy when 20 wt % HEA is added. These stages are accompanied by clearly identifiable slip bands that exhibit a variety of morphologies. The incorporation of high-entropy alloy into TA15 alloy leads to a decline in the occurrence of slip bands on the sample's surface. The decrease in slip bands and the rise in the quantity

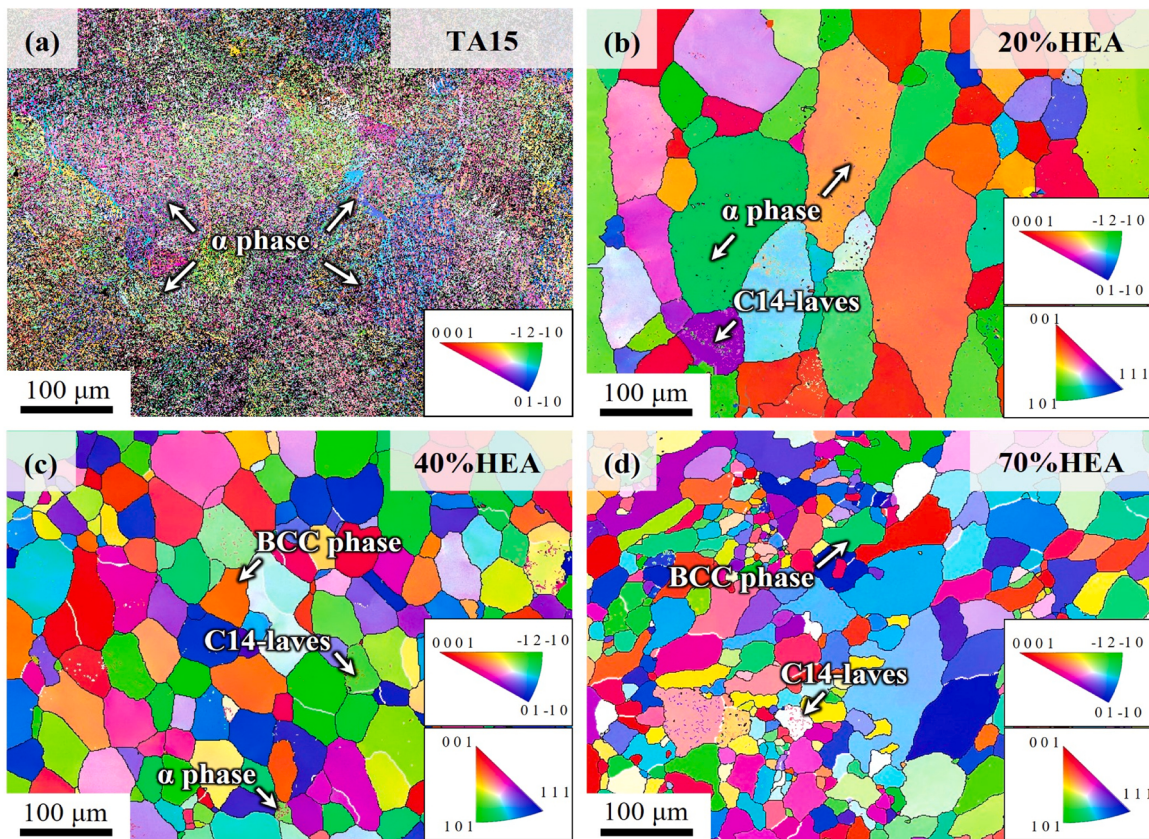


Fig. 5. EBSD images of HEA/Ti composite alloys with: (a) TA15, (b) 20_HEA, (c) 40_HEA, (d) 70_HEA.

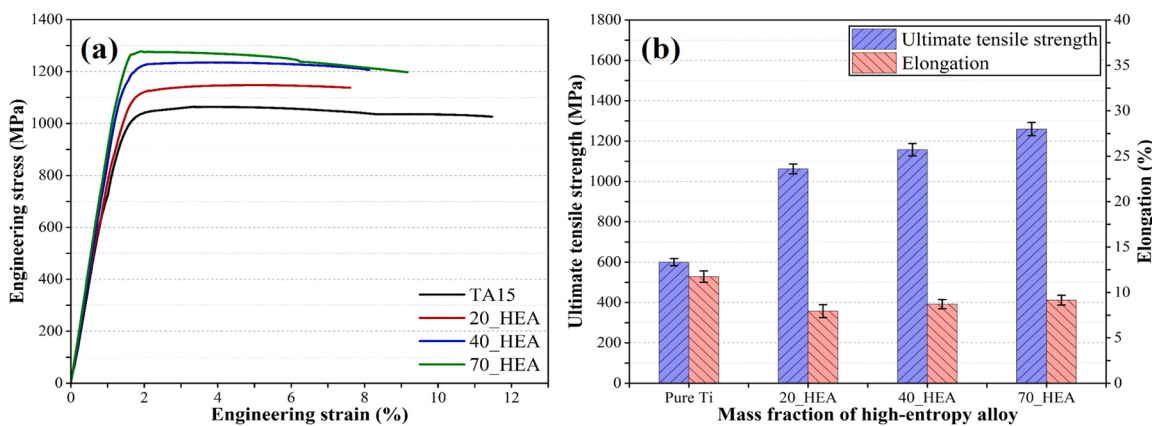


Fig. 6. Tensile property of HEA/Ti composite alloy with different proportion of high-entropy alloy added.

of deformed grains suggest a potential alteration in the material's deformation mechanism. More precisely, when a material has the ability to absorb and distribute a greater amount of deformation energy inside its grains, it indicates that the material is more capable of adjusting to external loads through deformation rather than breaking. The presence of fewer slip bands and a higher number of deformed grains may indicate a transition in the deformation mechanism from basic slip to plastic deformation occurring within the grains. Instead, small distorted particles align themselves with the direction of stretching. Nevertheless, the grains do not display any discernible deformation due to their inherent brittle fracture properties. Increasing the proportion of high-entropy alloy to 70 % results in significant plastic deformation inside the grains, which aligns with the direction of the tensile strain and improves ductility. Furthermore, several slip bands can be noticed at the root of

the notch. Similarly, notched specimens of the pristine high-entropy alloy exhibit intergranular fracture characteristics, where observable cracks form at the interfaces between individual grains.

Fracture shapes commonly observed in Fig. 8 are evident in tension samples with different proportions of high-entropy alloy. The fracture cross-section of the TA15 deposit shows a combination of ductile and brittle characteristics, as evidenced by the presence of large cleavage steps. These steps are accompanied by numerous small ductile dimples on their surfaces. Fig. 8b demonstrates that the inclusion of 20 wt % high-entropy alloy in titanium alloy leads to a significant reduction in the depth of the dimples on the step surfaces, while still retaining the presence of cleavage steps. This decrease aligns with the observed inclination of the fracture curve.

Nevertheless, as the high-entropy alloy level reaches 40 %, both the

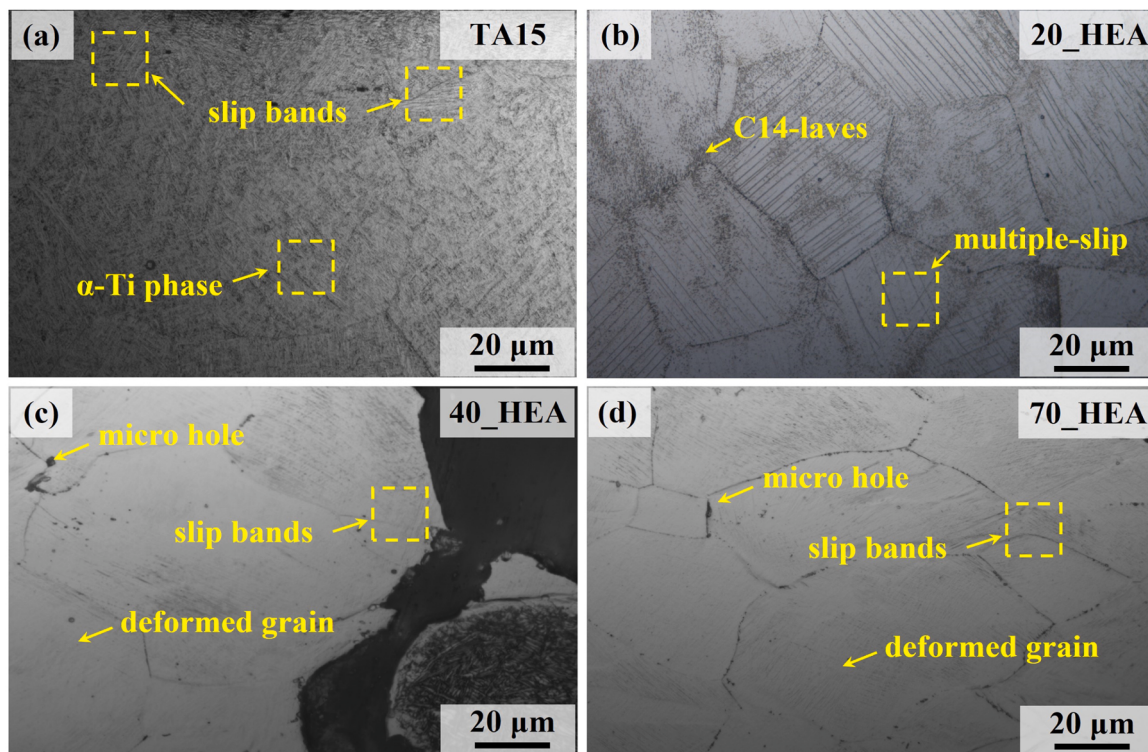


Fig. 7. Optical micrograph of titanium matrix complicated alloys with different content of high-entropy alloys: (a) TA15 alloy; (b) 20_HEA; (c) 40_HEA(c) 70_HEA.

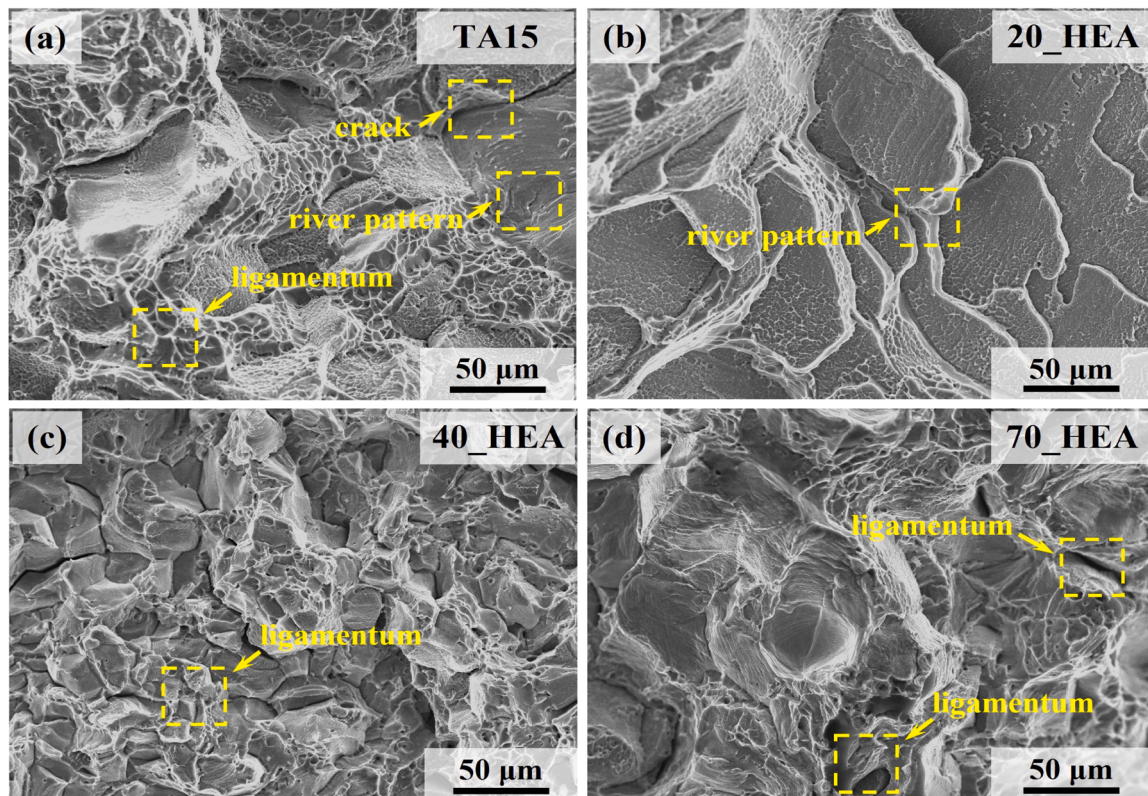


Fig. 8. SEM fracture morphologies images of HEA/Ti composite alloys with different content of high-entropy alloys added in: (a) TA15 alloy, (b) 20_HEA, (c) 40_HEA, (d) 70_HEA.

dimensions and extent of the dimples on the fracture cross-section expand, suggesting an enhancement in the malleability of the deposit at a high-entropy alloy content of 40 %. This pertains to the reduction in

the proportion of the HCP phase and the augmentation in the proportion of the BCC phase in the titanium alloy. Excessive amounts of high-entropy alloy in the deposit can cause the deposit to become more

brittle. This is particularly true for pure high-entropy alloy, where the fracture location shows cleavage steps and small, shallow dimples during the tensile process. These observations indicate a transition from ductile to brittle deformation mode.

4. Discussion

4.1. Effect of element on titanium composite

The microstructure depicted in Fig. 4 demonstrates that the incorporation of high-entropy alloy causes a progressive conversion of the columnar grains in TA15 into cellular or equiaxed grains. The occurrence of this phenomena can be ascribed to the impact of high-entropy alloy powder on the process of nucleation and growth inside the molten pool. During the laser melting process, a fraction of the laser energy is utilised to liquefy the TA15 alloy and high-entropy alloy powder, while another fraction penetrates the previously liquefied layer to create the molten pool. Partially liquefied powder particles that enter the molten pool act as points where nucleation occurs, resulting in the formation of equiaxed dendrites with random orientations at the upper section of the molten pool. High-entropy alloys possess a relatively large specific heat capacity due to the presence of numerous elements and a complex microstructure [37]. An increase in the fraction of high-entropy alloy leads to an increase in the overall specific heat capacity of the metal powder. As a result, the rate at which the material cools and the extent of unevenness diminish, making it easier for equiaxed and cellular dendrites to develop. The microstructure analysis in Section 3.2 demonstrates that the grain size of the titanium alloy is significantly reduced when high-entropy alloys are added. The phenomenon can be attributed to the influence of refractory elements, such as Nb and V, on the movement of grain boundaries during the process of grain formation in high-entropy alloys. The increase in the energy required for grain boundary migration leads to a decrease in the size of the microstructure in the deposited layer.

Fig. 9 illustrates the conversion of the α phase to the BCC phase with an increasing mass fraction of the high-entropy alloy. The phases were determined and analyzed using the CALPHAD (Calculation of Phase Diagrams) technique to forecast the equilibrium relationships following the introduction of the Nb element into the system. This facilitates the assessment of the microstructural changes in composite alloys containing different proportions of the Nb element. The enthalpies of mixing for the deposition layers containing different mass fractions of high-entropy alloys, specifically 20_HEA, 40_HEA, and 70_HEA, are -12.35 kJ/mol , -12.65 kJ/mol , and -12.94 kJ/mol , respectively. According to the criterion, it is clear that the mixing enthalpy decreases significantly

when high-entropy alloys are included, in comparison to the TA15 alloy. Furthermore, the mixing entropy of the deposition layer exhibits an increase, surpassing a value of $2.07 \times 10^{13} \text{ J}\cdot\text{mol}^{-1}\cdot\text{K}^{-1}$ [38], subsequent to the incorporation of high-entropy alloys. This suggests an increasing tendency in the creation of solid solution phases in the deposition layer. The introduction of a high entropy alloy into the titanium alloy results in the ionization of the atoms of each element. The lattice of the α phase undergoes expansion due to the incorporation of certain Nb atoms into the α -Ti lattice. Under high-energy beam stimulation, specific α phases transforms into β -Ti, and a small proportion even immediately transits into the body-centered cubic (BCC) phase, with an increased concentration of Nb elements in this region. The formation of the Laves phase involves the migration of Zr, Al, and V elements to the grain boundary location. Since the enthalpy of production of the Laves phase is lower (-5508.9 eV) compared to the body-centered cubic (BCC) structure (-3250.37 eV), it enhances the likelihood of its production and leads to the simultaneous presence of the α and Laves phases in the ultimate microstructure. As the mass fraction of high-entropy alloys (HEAs) in the titanium alloy increases, the volume fraction of the β phase grows due to the higher quantities of Nb elements. The body-centered cubic (BCC) phase is generated upon reaching the phase transition critical point of the β phase, facilitated by laser energy. In homogeneous high-entropy alloys (HEAs), the fine-grained Laves phase gradually merges to create a network-like, uninterrupted grain boundary. Simultaneously, Zirconium (Zr) and Aluminum (Al) atoms aggregate amidst dendrites, resulting in the formation of a granular C14 Laves phase.

The presence of Zr atoms at the grain boundary site leads to the expansion of the close-packed hexagonal lattice in the Laves phase. Throughout the process, the movement of energy associated with migration restricts the movement of the grain boundary. The influence of Zr atoms on the energy required for grain boundary migration can be mathematically described by the following formula:

$$\Delta E = \Delta E_0 + \Delta E_1 * C + \Delta E_2 * C^2 \quad (2)$$

Here, ΔE_0 represents the fundamental energy required for migration. In the formula, ΔE_1 and ΔE_2 are the coefficients that measure the impact of Nb element concentration C on the first and second order, respectively. ΔE represents the increase in energy required for grain boundary movement.

The formula demonstrates that the relationship between the concentration of the Nb element and the energy required for grain boundary movement is not linear. With a rise in the concentration of Nb element, the energy required for grain boundary movement also increases. The presence of the Nb element impacts the structure and stability of the grain boundary, resulting in increased difficulty for grain boundary migration.

4.2. Strengthening mechanisms of tensile property

Unlike the body-centered cubic (BCC) matrix phase, the Laves phase is characterized by a highly compact hexagonal structure that exhibits greater toughness. Furthermore, the formation of the Laves phase is the highest point of a matrix dislocation. An increase in the high entropy alloy component leads to the formation of more Laves phases. Moreover, the high entropy alloy exhibits a greater surface hardness compared to the TA15 alloy. In addition, the introduction of Zr atoms with larger atomic radii leads to an increase in the size disparity between the solute atoms, hence intensifying lattice deformation. Within the solid solution, this leads to a significant deformation in the lattice structure, resulting in a localized elastic stress field. The dislocation lines undergo bending due to the interaction between the elastic stress field and the dislocation stress field of the alloy, which hinders the movement of dislocations and enhances solid solution strengthening. Furthermore, the use of Zr elements enhances the grain refinement and increases the hardness of the

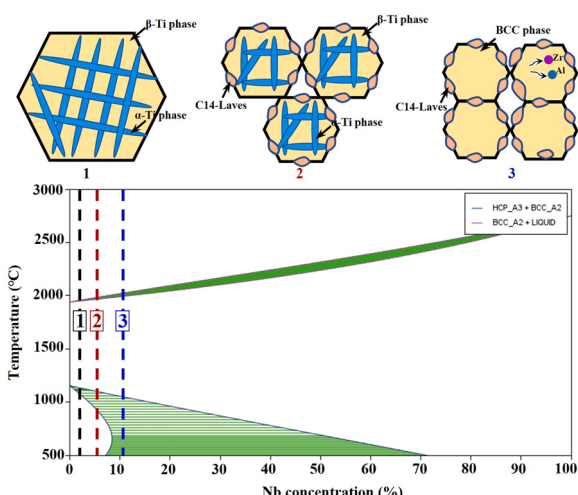


Fig. 9. Generated phases and phase diagram of the HEA/Ti composite alloys.

alloy by the reduction of grain size.

The three primary mechanisms of metal material strengthening are solid-solution strengthening, second-phase strengthening, and fine-grain strengthening. There is no laves phase and the grains are comparatively coarser than 90 μm in TA15 alloy. The precipitation strengthening supplied by the C14 Laves phase generated at the grain boundary is the primary mechanism of strengthening when 20 % of high-entropy alloy is added to TA15 alloy. V appears to have promoted the formation of the ZrAlV-type C14 Laves phase due to its stronger affinity for Al than Nb as the proportion of high-entropy alloy added to TA15 alloy improved to 70 % [39,40]. This was achieved by trapping Al into ZrAl-rich phases, specifically Zr₅Al₃-type and ZrAlV-type C14 Laves. The C14 Laves phase, which forms at the grain boundary, provides precipitation strengthening, which is the primary mechanism of the strengthening. The elastic interaction between the local stress field of the dislocation and the local stress field of the solute atoms is the reason behind the strengthening of solid solutions in HEAs.

Within the set of elements Al, Ti, V, Zr, Nb, and Mo, V has the smallest atomic radius, while Zr possesses the highest atomic radius. The shear modulus of these two elements is the highest, and they have the most significant impact on solid solution strengthening in alloys. Table 1 displays the variations in atomic size among the elements in multi-principal element alloys. When a small quantity of high-entropy alloy powder is introduced into the TA15 alloy matrix, the Al and Zr elements, which possess a high shear modulus, face challenges in functioning as solute atoms within the α -Ti lattice. Conversely, elements like Nb and Mo have the ability to integrate into the α -Ti structure by substituting certain Ti atoms. Consequently, α -Ti undergoes a transformation into β -Ti, and a minor portion of the β -Ti lattice further undergoes a transition into the body-centered cubic (BCC) phase, which contains a higher concentration of Ti, Nb, and V elements. Simultaneously, the elements Zr, V, and Al gather at the interfaces between grains, resulting in the formation of Laves phases. The high shear modulus of aluminum (Al) and zirconium (Zr) components poses a challenge for dislocations to traverse the grain boundaries. The intricate system including the high-entropy alloy and TA15 alloy can be regarded as distinct binary solute-solvent systems at various places. Table 2 displays the measurements of lattice distortion and shear modulus for the constituent elements in the high-entropy alloy. By examining the table, it is evident that the elements Nb and Mo exhibit a greater degree of lattice distortion in the matrix phase, classifying them as solute elements. On the other hand, the element Ti, which exhibits minimal lattice distortion, can be considered as a solvent. The maximum shear modulus is achieved during the Laves phase due to the presence of Al and V elements near the grain boundaries. These elements are classified as solute elements. On the other hand, Zr elements can be called solvents since they cause lattice distortion. The lattice distortion of the alloy can be understood as the elastic interaction between the lattice distortion surrounding V and Mo elements in the matrix phase and the lattice distortion surrounding Zr and Al elements at the grain boundaries.

The formulas (2) to (5) illustrate the calculation for lattice distortion and shear modulus.

$$\delta_a \approx \frac{c_V \delta_{av} + c_{Zr} \delta_{azr}}{c_V + c_{Zr}} - \frac{c_{Al} \delta_{aAl} + c_{Ti} \delta_{aTi} + c_{Nb} \delta_{aNb} + c_{Mo} \delta_{aMo}}{c_{Al} + c_{Ti} + c_{Nb} + c_{Mo}} \quad (2)$$

Table 2
Relative atomic size difference between alloying elements.

Element	Ti	Al	Nb	V	Zr	Mo
Ti	0	0.03	0.01	0.09	-0.08	0.08
Al	-	0	-0.02	0.06	-0.11	0.05
Nb	-	-	0	0.09	0.09	0.07
V	-	-	-	0	-0.18	0.01
Zr	-	-	-	-	0	0.16
Mo	-	-	-	-	-	0

Table 3

Relative modulus difference, δ_{Gij} , of the alloying element pairs.

Element	Ti	Al	Nb	V	Zr	Mo
Ti	0	0.5143	-0.1463	0.0659	0.8931	-0.0021
Al	-	0	0.3750	0.5753	1.2624	1.0936
Nb	-	-	0	-0.2118	-1.0065	0.5923
V	-	-	-	0	0.8395	0.0869
Zr	-	-	-	-	0	0.2594
Mo	-	-	-	-	-	0

$$\delta_a \approx \frac{c_{Al} \delta_{GAl} + c_{Zr} \delta_{GZr}}{c_{Al} + c_{Zr}} - \frac{c_{Ti} \delta_{GTi} + c_V \delta_{GV} + c_{Nb} \delta_{GNb} + c_{Mo} \delta_{GMo}}{c_{Ti} + c_V + c_{Nb} + c_{Mo}} \quad (3)$$

$$\Delta\sigma = \sqrt[3]{2AG_c^{\frac{2}{3}}\delta^{\frac{4}{3}}} \quad (4)$$

$$\sigma_{0.2} = (\sigma_{0.2})_{\text{mix}} + \Delta\sigma_a + \Delta\sigma_G \quad (5)$$

Where δ_{av} and δ_{GV} indicate the lattice distortion and shear modulus of element V, respectively, as determined by the Senkov model. The Senkov model postulates that the local atomic concentration is equivalent to the average atomic concentration. Additionally, it considers the distortion of the lattice of an element as a result of the disparity between the atomic size and modulus of the element and its closest neighboring elements.

$$\delta_{ai} = \frac{16}{8} \sum c_j \delta_{aj} \quad (6)$$

$$\delta_{Gi} = \frac{16}{8} \sum c_j \delta_{Gij} \quad (7)$$

Where, c_j is the atomic fraction of element j in alloy a, 16 is the number of atoms in the i-centered cluster in the BCC lattice, 8 is the number of atoms neighboring the central atom i, $\delta_{ij} = 2(r_i - r_j)/(r_i + r_j)$ represents the difference in atomic sizes between elements i and j. Similarly, the modulus distortion δ_{Gij} , estimated around element i, is given by the modulus distortion of element i and $\delta_{Gij} = 2(G_i - G_j)/(G_i + G_j)$.

4.3. Dislocation pileup at phase boundary

The EBSD data is integrated with the geometrically required dislocation (GND) density diagrams of titanium complex alloys including varying proportions of high entropy alloys, as shown in Fig. 10. As the mass fraction of high entropy alloys added to TA15 alloy rises, the average GND density of the specimens also increases. The average GND value is utilized to represent the distribution of dislocations in the specimens. The expression of ground nodes (GNDs) can be represented using the KAM value, which can be calculated using the following formula: $\rho^{\text{GNDs}} = 2\text{KAMave}/\mu b$ [41,42], where ρ is the GNDs density and b is the length of the Burgers vector ($1/3 <1120>$ was used to calculate, 0.295 nm for titanium). The dislocation densities of TA15 alloy, 20_HEA, 40_HEA, 70_HEA, and pure HEA were calculated as $1.875 \times 10^{14} \text{ m}^{-2}$, $1.94 \times 10^{14} \text{ m}^{-2}$, $2.45 \times 10^{14} \text{ m}^{-2}$, and $2.065 \times 10^{14} \text{ m}^{-2}$ and $2.165 \times 10^{14} \text{ m}^{-2}$ respectively, which are consistent with the tensile results in Fig. 6. Therefore, the improvement in plasticity of the 70_HEA and 40_HEA samples compared to the 20_HEA can be understood as the softening behavior resulting from an increase in the slip systems between the BCC cubic structure and the α -phase hexagonal structure. The significant increase in strength of the samples compared to TA15 alloy is attributed to the higher dislocation density caused by the noticeable difference in lattice structures between the BCC phase and the α -phase. The alloy's strength can be increased by lattice distortion, and the activation of several slip systems at the same time reveals the process by which the material becomes softer. The TA15 alloy predominantly engages the prismatic plane slip system at normal room temperature. By incorporating a suitable quantity of high-entropy alloy, the presence of

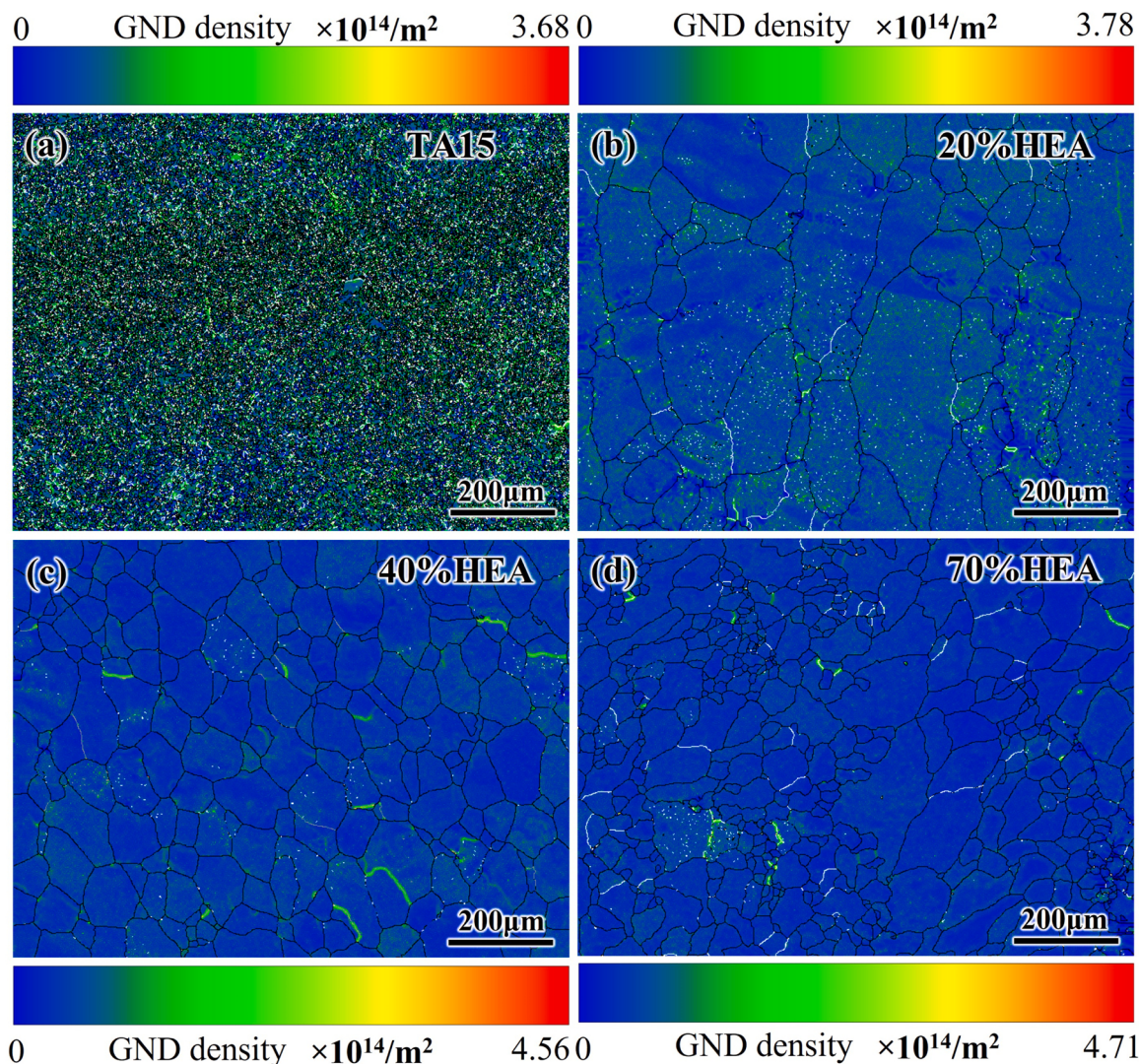


Fig. 10. KAM and GND of titanium composite alloys with different fractions of high entropy alloys added: (a) TA15, (b) 20_HEA, (c) 40_HEA, (d) 70_HEA.

slip systems like [1 1 0] in the cubic structure facilitates the movement of dislocations across phase boundaries, enabling the initiation of the slip system even under low stress.

Fig. 10a illustrates that the dislocations in TA15 are primarily concentrated at the interfaces between α phases. This is due to the fact that the α phase has a close-packed hexagonal structure, and the deformation slip predominantly occurs through the activation of prismatic slip systems. The TA15 alloy is classified as an α -type titanium alloy, mostly composed of the α phase as the matrix phase with Al elements as dopants. The content of the β phase, which is doped with V and Mo elements, is quite minimal. The α phases exhibit a notable level of coherence among themselves, and the dislocation crossing of the phase interface occurs with relative ease. Nevertheless, the introduction of a minute quantity of high-entropy alloy into the TA15 alloy results in the formation of a Laves phase predominantly consisting of Zr-Al within the matrix phase. While the Laves phase and the α phase share a close-packed hexagonal structure, the introduction of elements like Zr and V with atomic radii that differ significantly from those of Al atoms in the lattice can lead to expansion or contraction of the α phase. This disrupts the coherence between certain α phases and makes it more challenging for dislocations to cross the phase interface. Consequently, there is an increase in the geometrically necessary dislocation density at the phase interface. As the amount of high-entropy alloy added to the TA15 alloy increases, the concentration of β -phase stabilizing elements like Nb and

V also increases. Consequently, the proportion of the β phase within the matrix phase gradually rises. This disrupts the coherence between the α and β phases, making the phase interface between them the primary hindrance for dislocation slip.

At a high proportion of 70 %, the addition of high-entropy alloy to the TA15 alloy causes a transformation of the matrix phase from α to β . Despite an increase in slip systems in the body-centered cubic structure, the slow diffusion of high-entropy alloy hinders the solid solution process of elements like Nb and V in the matrix. As a result, various body-centered cubic phases with different structures appear in the matrix, and their coherence is suppressed. Simultaneously, the Laves phase is distributed throughout the matrix phase, resulting in a substantial increase in dislocation density inside the deposited layer. This increase is approximately 50 % greater than that observed in the titanium alloy. Meanwhile, in Fig. 10d, it can be observed that the pure high-entropy alloy exhibits a high density of dislocations. However, the presence of a network-like Laves phase at the boundaries between grains leads to a more severe accumulation of dislocations at these positions. This, in turn, greatly diminishes the ability of the deposition layer to undergo plastic deformation and reduces its strength at room temperature.

4.4. Fracture toughness criterion of the mechanical deformation

In the case of conventionally treated TA15 alloys, the shift from

body-centered cubic (BCC) to orthorhombic phase occurs at grain boundaries. These boundaries are distinguished by their high interfacial energy and significantly less strong bonding. The C14 Laves phases formed during the DED process act as brittle second phases, causing plastic strain incompatibility at the interfacial area. The plastic strain incompatibility results in the buildup of Kernel Average Misorientation (KAM) at the interfaces, as depicted in Fig. 10. The cumulative KAM value suggests the existence of a significant quantity of high-energy geometrically required dislocations (GNDs).

The stress-strain curve depicted in Fig. 7 demonstrates that the TA15 samples, which underwent in-situ alloying, had a tensile strength of 1189.2 MPa. Furthermore, the 20_HEA sample, characterized by a higher Nb content during the DED process, exhibits a tensile strength that is 12.3 % greater. Despite the comparatively high grain size (81.8 μm) of the 20_HEA samples, their current tensile strength is equivalent to the values obtained from tensile tests conducted on TA15 samples. The exceptional strength of the HEA/Ti composite samples, achieved through in-situ alloying, can be attributed to their heterogeneous microstructure and transformation-induced plasticity (TRIP) behavior. The laser additive manufacturing process results in a diverse microstructure in the samples, which enhances their strength by increasing the dislocation density at the interface regions, including cell structures, inclusions, and second phases. The deformation microstructures displayed in Fig. 10 reveal a notable buildup of Kernel Average Misorientation (KAM) at the boundary between the C14 Laves phase and the α -Ti matrix. This accumulation of dislocation density boosts the strength of the material through mechanisms such as dislocation hardening and back stress hardening. The load transfer characteristic facilitates the initiation of yielding in the rigid matrix, leading to the reduction of tension and strain at the interface. Due to stress and strain relaxation at the interface, this sample exhibits great strength even though it has minor outward flaws. The local misorientation distribution, as depicted in Fig. 10b and c, reveals that there is a greater buildup of Kernel Average Misorientation (KAM) at the interface region between the laves phase and the BCC phase, in comparison to other regions of the matrix.

Furthermore, the samples that underwent in-situ alloying demonstrate reduced ductility, measuring approximately 6.8 %, when compared to the TA15 samples. This is clearly shown in the optical micrographs presented in Fig. 4. The fracture surfaces of the TA15 and 20_HEA samples, as shown in Fig. 8, indicate that crack start does not happen within the grains but rather at the borders during the tensile test. Moreover, the 70_HEA sample exhibits fewer sites of crack initiation compared to the 20_HEA sample. As seen in Fig. 8(a), the reduction of C14 Laves phase in the grain boundary can explain these data.

The majority of stress-strain curves follow a simple energy expression known as the Holloman equation, as follows:

$$\sigma = Ke^n \quad (8)$$

where σ is the true stress, ϵ is the true strain, K is the strength coefficient, and n is the strain hardening exponent. The Holloman equation is commonly used in materials science and engineering to characterize the mechanical behavior of materials under plastic deformation.

The hardening index, on the other hand, is a measure of the rate at which a material hardens during plastic deformation. It is often represented by the strain hardening exponent, n , in the Holloman equation. A higher value of n indicates a greater rate of hardening, meaning that the material becomes stronger and more resistant to deformation as the plastic strain increases.

The hardening index is an important parameter in materials processing and design, as it affects the formability, ductility, and strength of a material. It is often determined through experimental testing or can be estimated based on the material's microstructure and composition.

In order to determine the change in the hardening index throughout the tensile process of the deposited layer composed of various ratios of high-entropy alloys in TA15 alloy, the previously mentioned Holloman

stress-strain equation can be modified to derive Eq. (9). The impact of changes in the mass fraction of high-entropy alloys on the strain hardening exponent (n) is illustrated in Fig. 12.

$$\ln \sigma = \ln K + n \ln \epsilon \quad (9)$$

Based on the above equation, plotting $\ln \sigma$ against $\ln \epsilon$ as shown in Fig. 11, it can be observed that a smaller work hardening exponent (n) indicates a higher likelihood of yielding and work hardening in metal stretching, while a larger n suggests a greater tendency for brittle fracture or susceptibility to recrystallization softening. From the graph, it can be seen that when a 20 % high-entropy alloy is added to the TA15 alloy, the work hardening exponent decreases by 0.78 % compared to TA15 alloy. However, when the proportion of high-entropy alloy is increased to 60 %, the work hardening exponent during the tensile process increases by 1.46 % compared to the absence of high-entropy alloy.

From the graph in Fig. 6, it is clear that the addition of a tiny amount of $\text{Al}_{0.8}\text{Nb}_{0.5}\text{Ti}_2\text{V}_2\text{Zr}_{0.5}$ to the TA15 alloy leads to a significant drop in the elongation rate of the specimen. Furthermore, although necking is present at the microfracture location, brittle fracture remains evident. Hahn and Rosenfield have suggested an empirical formula to accurately characterize the fracture toughness of materials at room temperature. [43]:

$$K_{IC} = n \left(\frac{2E\sigma_y \epsilon_f}{3} \right)^{\frac{1}{2}} \quad (10)$$

Where n is the hardening exponent, E is the elastic modulus (MPa), σ_y is the yield stress (MPa), and ϵ_f is the true fracture strain under uniaxial tension. The fracture toughness of the specimens with varying amounts of high-entropy alloy is determined using Eq. (2), as seen in Fig. 12. When the proportion of high-entropy alloy in the multi-principal element alloy is less than 20 %, the fracture toughness index experiences a notable reduction in comparison to the TA15 alloy. When the weight ratio of high-entropy alloy reaches around 65 %, the fracture toughness of the specimens tends to reach a stable state. The fracture toughness of TA15 alloy at room temperature is determined to be $117.12 \text{ MPa}\cdot\text{m}^{1/2}$ in this experiment. Typically, the highest fracture toughness of titanium alloys at normal temperature is $100 \text{ MPa}\cdot\text{m}^{1/2}$ [44]. The fracture toughness of the specimens containing 20 wt % of high-entropy alloy (HEA) is measured to be $103.65 \text{ MPa}\cdot\text{m}^{1/2}$. The fracture toughness index increases to $111.90 \text{ MPa}\cdot\text{m}^{1/2}$ when the high-entropy alloy concentration is 70 wt %. This suggests that the deliberate inclusion of high-entropy alloy can improve the resistance of cracks spreading and the toughness of the specimens. However, the fracture toughness of the specimens experiences a substantial drop when the mass fraction of HEA reaches 20 %. The observation suggests a pattern of crack growth and structural failure in the fracture specimen 20_HEA. The inset in Fig. 12, namely in region I, illustrates the deformation and fracture mode of the specimen 70_HEA. The findings indicate that in addition to the evident twinning and distortion of the grain structure, the grain borders also demonstrate substantial plastic deformation. Both the individual grains and the interfaces between them experience specific forces throughout the tensile process. Grain boundaries can effectively enhance the strength. Consequently, microvoids and fissures are generated inside the grains. Fortunately, the process of layering serves to keep the cracks from expanding and also enhances the fracture toughness of the specimen.

The figure contained in Fig. 10 demonstrates that at normal ambient temperature, grain boundaries containing the C14 Laves phase are susceptible to the initiation and spread of cracks. Moreover, cracks have a tendency to merge and create primary cracks, which subsequently result in failure at the interfaces between grains. The strength of the grains surpasses that of the grain boundaries, since the grains exhibit no deformation, while cracks initially manifest at the grain boundaries. Moreover, the shift from the prevailing strength of grain boundaries to

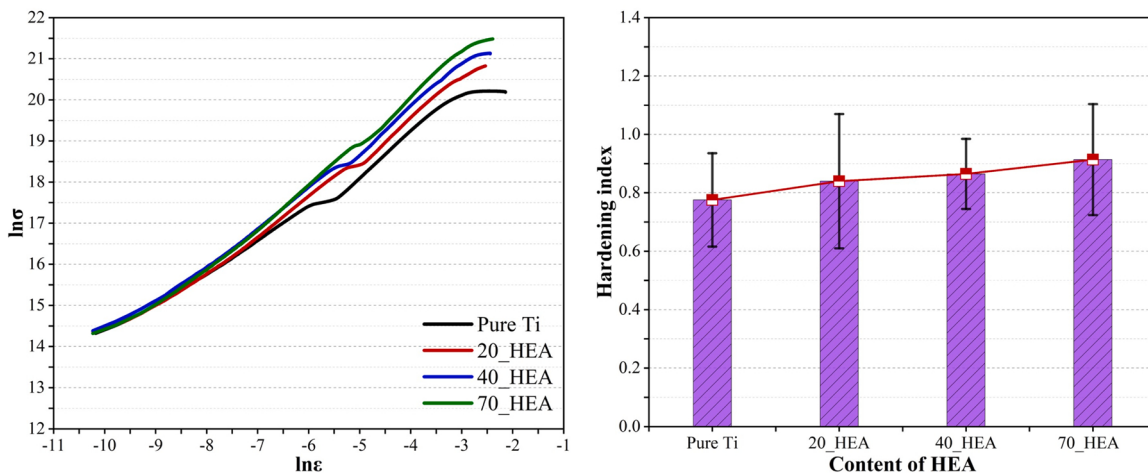


Fig. 11. Fracture toughness index of titanium matrix complicated alloys with different content of high-entropy alloys.

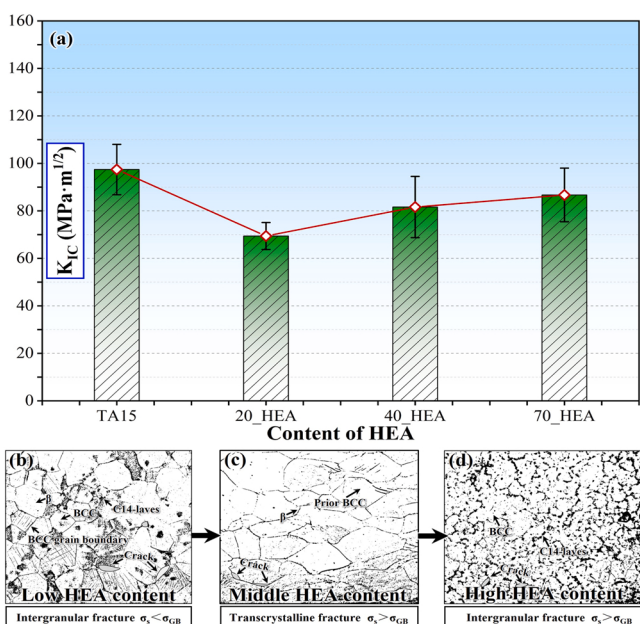


Fig. 12. Variation trend of fracture toughness with content of high-entropy alloy and schematic diagram of fracture mode.

the prevailing strength of individual grains takes place during the transitional phase of the respective samples, ranging from 20 wt % HEA to 70 wt % HEA. In the specimen containing 70 wt % HEA, the stress condition at the triple point of the grain boundaries resembles the triaxial tensile stress condition. This similarity arises because the occurrence of wedge crack formation is heightened by the occurrence of multiple grain boundary sliding. As per Riedel's proposed expression, the stress distribution at grain boundaries can be determined [45].

$$\sigma = 0.25\sigma_{\infty} \left[\frac{d}{r} \right]^{1/2} \quad (11)$$

Where, d represents the grain diameter, σ_{∞} represents the external force, and r represents the distance from the three critical points. Fig. 12 demonstrates that with an increase in grain size and a decrease in distance from the three critical locations, the stress level rises, hence increasing the susceptibility to the production of microvoids. The findings indicate that stress aligns with the rough β and BCC grain boundaries, with the three key locations being in close proximity to one other.

The formation and merging of microvoids are likely to occur within the primary crack. The size of the crack development is intricately linked to the fracture mode of the specimen, as per the principles of linear elastic fracture mechanics theory.

The fracture toughness of a plate with a central penetrating crack of finite width can be stated as follows.

$$\alpha = \left[\frac{K_{IC}}{\sigma \left(\frac{a}{W} \right)} \right]^2 \cdot \frac{1}{\pi} \quad (12)$$

Where a is the crack half-length (in millimeters), W is the width of the specimen (in millimeters), and σ is the yield strength (in megapascals). By utilizing Eq. (12), the calculated unstable critical half-length of the 70_HEA specimen at room temperature is 126.5 μm , which closely approximates the maximal β size prior to the specimen. Cracks can readily develop at the interfaces between grains and propagate beyond the length threshold where they become unstable. Put simply, once the primary crack is created, it is susceptible to brittle fracture and subsequent failure.

5. Conclusion

In the present work, multi-principal element alloys were prepared by laser melting deposition. The effect of high entropy alloy content added in TA15 alloy on microstructure and mechanical properties of titanium matrix complicated alloys was studied. Based on the results and analysis, the following conclusions are drawn:

- 1) The promotion in the content of high-entropy alloy in the TA15 alloy leads to an increase of elements such as Nb and V, which inhibits the grain boundary migration process and results in significant refinement of the microstructure in the alloy. When the mass fraction of high-entropy alloy in the alloy reaches 20 wt %, the average grain size in the deposition layer decreases by approximately 37.90 %. Furthermore, 70 wt % of high-entropy alloy even reduces the grain size of the TA15 alloy to half of its original size.
- 2) Comparing the mechanical properties of 0_HEA and 60_HEA, the value of tensile strength at room temperature increased from 1085 MPa to 1235 MPa. The tensile strain at room temperature decreased from 12.9 % to 8.72 %.
- 3) The main matrix phase in TA15 alloy is α -Ti phase, the addition of HEA particles leads to an increase in the volume fraction of β phase and BCC phase in the composite. With the promotion of high entropy alloys from 0 wt % to 70 wt %, the volume fraction of the α -Ti phase decreases and the BCC phase increases. The fracture mode of TA15

alloy is an intergranular fracture by the transformation of precipitation and matrix phases. When the mass fraction of high entropy alloy added in TA15 alloy is between 20 wt % and 70 wt %, the alloys exhibit a remarkable balance between strength and ductility.

Overall, the impact of different ratios of high-entropy alloy on the microstructure and mechanical properties of titanium alloy composites was examined. The composition ratios that have been researched may not be directly applicable to the production of crucial high-temperature bearing components for spacecraft. Nevertheless, this study highlights the importance of solid solution phases and intermetallic compounds in influencing the microstructural changes in multi-principal element alloys. This knowledge is valuable for creating lightweight gradient materials that can be used in high-temperature structural applications in aircraft.

CRediT authorship contribution statement

Xiaohong Zhan: Supervision, Resources, Project administration. **Linqin Li:** Validation. **Leilei Wang:** Project administration, Methodology. **Longxiang Sun:** Visualization, Validation, Investigation. **Yiqing Zhao:** Writing – review & editing. **Yumeng Zhang:** Writing – original draft, Investigation, Formal analysis, Conceptualization.

Declaration of Competing Interest

The authors declared that they have no conflicts of interest to this work. We declare that we do not have any commercial or associative interest that represents a conflict of interest in connection with the work submitted.

Data Availability

No data was used for the research described in the article.

Acknowledgments

The authors gratefully acknowledge the financial support of the Defense Industrial Technology Development Program [grant number JCKY2022605C004].

References

- [1] X. Liu, H. Gao, H. Wu, H. Pan, B. Shu, Y. Yang, H. Liu, F. Yang, X. Zhu, Microstructure and texture characteristics of pure Ti with a superior combination of strength and ductility, *Mater. Sci. Eng. A* 808 (2021) 140915, <https://doi.org/10.1016/j.msea.2021.140915>.
- [2] A. Yin, W. Yu, W. Zhu, W. Li, V. Ji, C. Jiang, Microstructural characterization and wear performance of shot-peened TA15 titanium alloy fabricated by SLM, *Mater. Charact.* 209 (2024) 113747, <https://doi.org/10.1016/j.matchar.2024.113747>.
- [3] S. Li, S. Li, L. Liu, H. Liu, C. Wang, P.J. Withers, Y. Zhu, L. Gao, S. Wang, B. Chen, W. Huo, J. Gao, X. Zhang, B. Li, High-temperature “Inverse” Hall-Petch relationship and fracture behavior of TA15 alloy, *Int. J. Plast.* 176 (2024) 103951, <https://doi.org/10.1016/j.ijplas.2024.103951>.
- [4] D. Zhu, J. Yan, Y. Jin, D. Dong, X. Wang, T. Ma, Pressure-induced excellent corrosion resistance of Ti-45Al-8Nb alloy, *Mater. Lett.* 355 (2024) 135446, <https://doi.org/10.1016/j.matlet.2023.135446>.
- [5] S.J. Han, G.B. Bang, W.R. Kim, G.H. Kim, H.-S. Kang, H.S. Han, T.W. Lee, H.G. Kim, Effect on microstructural and mechanical properties of selective laser melted pure Ti parts using stress relief heat-treatment process, *J. Mater. Res. Technol.* 27 (2023) 200–208, <https://doi.org/10.1016/j.jmrt.2023.09.288>.
- [6] C. Guo, G. Dai, J. Niu, Y. Guo, Z. Sun, H. Chang, Q. Zhang, Fe nanoparticles modified pure Ti alloy on microstructure evolution and fine crystallization mechanism fabricated by additive manufacturing, *J. Mater. Res. Technol.* 26 (2023) 5860–5872, <https://doi.org/10.1016/j.jmrt.2023.08.221>.
- [7] J. Zhang, X. Xu, J. Xue, S. Liu, Q. Deng, F. Li, J. Ding, H. Wang, H. Chang, Hot deformation characteristics and mechanism understanding of Ti-6Al-2Sn-4Zr-6Mo titanium alloy, *J. Mater. Res. Technol.* 20 (2022) 2591–2610, <https://doi.org/10.1016/j.jmrt.2022.08.044>.
- [8] E. Zhao, S. Sun, Y. Zhang, Recent advances in silicon containing high temperature titanium alloys, *J. Mater. Res. Technol.* 14 (2021) 3029–3042, <https://doi.org/10.1016/j.jmrt.2021.08.117>.
- [9] Z. Ye, X. Zhou, F. Zhang, K. Wang, K. Zhao, Z. Yu, Y. Wang, H. Tan, Effects of process parameters on the microstructure and mechanical properties of a laser micro-alloying TiB/Ti-6Al-4V titanium matrix composite, *Mater. Sci. Eng. A* 873 (2023) 144988, <https://doi.org/10.1016/j.msea.2023.144988>.
- [10] Y. Hu, Z. Hua, G. Mi, M. Zhang, Z. Liu, X. Zhang, X. Yan, C. Wang, Investigation on the evolution of deposition layer grain structure and its effect on mechanical properties in aluminum alloy fabricated by laser directed energy deposition, *Mater. Sci. Eng. A* 892 (2024) 145866, <https://doi.org/10.1016/j.msea.2023.145866>.
- [11] A. Gonnabattula, R.S. Thanumoorthy, S. Bontha, A.S.S. Balan, V.A. Kumar, A. K. Kanjrala, Process parameter optimization for laser directed energy deposition (LDED) of Ti6Al4V using single-track experiments with small laser spot size, *Opt. Laser Technol.* 175 (2024) 110861, <https://doi.org/10.1016/j.optlastec.2024.110861>.
- [12] W. Jeong, Y.-B. Chun, S.H. Kang, C.K. Rhee, C.H. Yoo, S. Yoo, H. Kim, M. Akmal, H. J. Ryu, Enhancement of strength and ductile-brittle transition temperature of SA508 Gr.3 low-alloy steel by controlling heat accumulation in laser powder-directed energy deposition, *J. Mater. Sci. Technol.* (2024), <https://doi.org/10.1016/j.jmst.2024.02.042>.
- [13] Z. Gao, L. Wang, Y. Wang, F. Lyu, X. Zhan, Crack defects and formation mechanism of FeCoCrNi high entropy alloy coating on TC4 titanium alloy prepared by laser cladding, *J. Alloy. Compd.* 903 (2022) 163905, <https://doi.org/10.1016/j.jallcom.2022.163905>.
- [14] Z. Hua, L. Xiong, M. Zhang, C. Wang, G. Mi, P. Jiang, Microstructure evolution and tribological properties of (TiB+TiC)/Ti-6Al-4V composites fabricated via in situ laser-directed energy deposition of wire and powders in an underwater environment, *Compos. B Eng.* 263 (2023) 110817, <https://doi.org/10.1016/j.compositesb.2023.110817>.
- [15] I.Y. Kim, B.J. Choi, Y.J. Kim, Y.Z. Lee, Friction and wear behavior of titanium matrix (TiB+TiC) composites, *Wear* 271 (2011) 1962–1965, <https://doi.org/10.1016/j.wear.2010.12.072>.
- [16] B.-J. Choi, I.Y. Kim, Y.-Z. Lee, Y.-J. Kim, Microstructure and friction/wear behavior of (TiB+TiC) particulate-reinforced titanium matrix composites, *Wear* 318 (2014) 68–77, <https://doi.org/10.1016/j.wear.2014.05.013>.
- [17] Y. Xiong, M. Du, F. Zhang, F. Saba, C. Shang, Preparation and mechanical properties of titanium alloy matrix composites reinforced by Ti3AlC and TiC ceramic particulates, *J. Alloy. Compd.* 886 (2021) 161216, <https://doi.org/10.1016/j.jallcom.2021.161216>.
- [18] F. Zhang, M. Du, K. Fan, C. Ye, B. Zhang, Fabrication and mechanical properties of network structured titanium alloy matrix composites reinforced with Ti2AlC particulates, *Mater. Sci. Eng. A* 776 (2020) 139065, <https://doi.org/10.1016/j.msea.2020.139065>.
- [19] Q. Zhang, W. Sun, S. Xu, X. Zhang, J. Wang, C. Si, Nano-TiB whiskers reinforced Ti-6Al-4V matrix composite fabricated by direct laser deposition: microstructure and mechanical properties, *J. Alloy. Compd.* 922 (2022) 166171, <https://doi.org/10.1016/j.jallcom.2022.166171>.
- [20] Y. Feng, Y. Lu, X. Liu, H. Cao, W. Wang, J. Yang, W. Chen, G. Cui, High strength and plasticity TiBw/TA15 composites with a novel columnar network structure, *Scr. Mater.* 229 (2023) 115349, <https://doi.org/10.1016/j.scriptamat.2023.115349>.
- [21] S. Wang, L. Huang, S. Jiang, R. Zhang, B. Liu, F. Sun, Q. An, Y. Jiao, L. Geng, Microstructure evolution and tensile properties of as-rolled TiB/TA15 composites with network microstructure, *Mater. Sci. Eng. A* 804 (2021) 140783, <https://doi.org/10.1016/j.msea.2021.140783>.
- [22] Z. Yuan, H. Liu, Z. Ma, X. Ma, K. Wang, X. Zhang, Microstructure and properties of high entropy alloy reinforced titanium matrix composites, *Mater. Charact.* 187 (2022) 111856, <https://doi.org/10.1016/j.matchar.2022.111856>.
- [23] F. Qiang, S. Xin, P. Guo, H. Hou, J. Wang, W. Hou, Formation mechanism of interdiffusion layer and mechanical properties of Al0.6CoCrFeNi high-entropy alloy/Ti composites, *J. Alloy. Compd.* 943 (2023) 169151, <https://doi.org/10.1016/j.jallcom.2023.169151>.
- [24] T. Xiang, P. Du, W. Bao, Z. Cai, K. Li, G. Xie, Bimodal grain size structure design to optimize the mechanical properties of TiZrNbTa high entropy alloys/Ti composites, *Mater. Sci. Eng. A* 849 (2022) 143488, <https://doi.org/10.1016/j.msea.2022.143488>.
- [25] S. Huang, Q. Zhao, Z. Yang, C. Lin, Y. Zhao, J. Yu, Strengthening effects of Al element on strength and impact toughness in titanium alloy, *J. Mater. Res. Technol.* 26 (2023) 504–516, <https://doi.org/10.1016/j.jmrt.2023.07.206>.
- [26] J. Zhang, H. Guo, M. Hu, H. Xu, H. Ju, D. Xu, C. Teng, R. Yang, Effect of common alloying elements on α' martensite start temperature in titanium alloys, *J. Mater. Res. Technol.* (2023), <https://doi.org/10.1016/j.jmrt.2023.10.159>.
- [27] A.-Y. Yu, H. Wei, Q.-M. Hu, R. Yang, Alloying element's substitution in titanium alloy with improved oxidation resistance and enhanced magnetic properties, *J. Magn. Magn. Mater.* 422 (2017) 20–24, <https://doi.org/10.1016/j.jmmm.2016.08.046>.
- [28] W. Zhang, A. Chabok, H. Wang, J. Shen, J.P. Oliveira, S. Feng, N. Schell, B.J. Kooi, Y. Pei, Ultra-strong and ductile precipitation-strengthened high entropy alloy with 0.5% Nb addition produced by laser additive manufacturing, *J. Mater. Sci. Technol.* 187 (2024) 195–211, <https://doi.org/10.1016/j.jmst.2023.11.053>.
- [29] S.-P. Wang, J. Xu, TiZrNbTa-Mo high-entropy alloys: dependence of microstructure and mechanical properties on Mo concentration and modeling of solid solution strengthening, *Intermetallics* 95 (2018) 59–72, <https://doi.org/10.1016/j.intermet.2018.01.017>.
- [30] X. Li, Z. Li, Z. Wu, S. Zhao, W. Zhang, H. Bei, Y. Gao, Strengthening in Al-, Mo- or Ti-doped CoCrFeNi high entropy alloys: a parallel comparison, *J. Mater. Sci. Technol.* 94 (2021) 264–274, <https://doi.org/10.1016/j.jmst.2021.02.060>.

- [31] Y. Fang, C. Liu, K. Jin, X. Wei, X. Zhao, H. Bei, Z. Zhang, Additive manufacturing of titanium alloys with enhanced strength and uniform ductility via multi-element alloying, *J. Mater. Res. Technol.* 24 (2023) 6854–6860, <https://doi.org/10.1016/j.jmrt.2023.04.239>.
- [32] J. Su, F. Jiang, C. Tan, F. Weng, F.L. Ng, M.H. Goh, H. Xie, J. Liu, Y. Chew, J. Teng, Additive manufacturing of fine-grained high-strength titanium alloy via multi-eutectoid elements alloying, *Compos. B Eng.* 249 (2023) 110399, <https://doi.org/10.1016/j.compositesb.2022.110399>.
- [33] W. Jiang, X. Wang, S. Li, T. Ma, Y. Wang, D. Zhu, A lightweight Al0.8Nb0.5Ti2V2Zr0.5 refractory high entropy alloy with high specific yield strength, *Mater. Lett.* 328 (2022) 133144, <https://doi.org/10.1016/j.matlet.2022.133144>.
- [34] N.Y. Yurchenko, N.D. Stepanov, S.V. Zherebtsov, M.A. Tikhonovsky, G. A. Salishchev, Structure and mechanical properties of B2 ordered refractory AlNbTiVZrx ($x = 0-1.5$) high-entropy alloys, *Mater. Sci. Eng. A* 704 (2017) 82–90, <https://doi.org/10.1016/j.msea.2017.08.019>.
- [35] S. Zeng, Y. Zhou, H. Li, H. Zhang, H. Zhang, Z. Zhu, Microstructure and mechanical properties of lightweight Ti3Zr1.5NbVALx ($x=0, 0.25, 0.5$ and 0.75) refractory complex concentrated alloys, *J. Mater. Sci. Technol.* 130 (2022) 64–74, <https://doi.org/10.1016/j.jmst.2022.05.005>.
- [36] Y. Zhang, H. Wang, Y. Zhu, S. Zhang, F. Cheng, J. Yang, B. Su, C. Yang, High specific yield strength and superior ductility of a lightweight refractory high-entropy alloy prepared by laser additive manufacturing, *Addit. Manuf.* 77 (2023) 103813, <https://doi.org/10.1016/j.addma.2023.103813>.
- [37] K. Li, J. Zhan, M. Zhang, R. Ma, Q. Tang, D.Z. Zhang, L.E. Murr, H. Cao, A functionally graded material design from stainless steel to Ni-based superalloy by laser metal deposition coupled with thermodynamic prediction, *Mater. Des.* 217 (2022) 110612, <https://doi.org/10.1016/j.matdes.2022.110612>.
- [38] X. Jin, Y. Zhou, L. Zhang, X. Du, B. Li, A new pseudo binary strategy to design eutectic high entropy alloys using mixing enthalpy and valence electron concentration, *Mater. Des.* 143 (2018) 49–55, <https://doi.org/10.1016/j.matdes.2018.01.057>.
- [39] X. Ma, X. Ding, R. Chen, W. Cao, Q. Song, Study on hydrogen storage property of (ZrTiVFe) x Al y high-entropy alloys by modifying Al content, *Int. J. Hydrot. Energy* 47 (2022) 8409–8418, <https://doi.org/10.1016/j.ijhydene.2021.12.172>.
- [40] S. Zherebtsov, N. Yurchenko, E. Panina, M. Tikhonovsky, N. Stepanov, Gum-like mechanical behavior of a partially ordered Al5Nb24Ti40V5Zr26 high entropy alloy, *Intermetallics* 116 (2020) 106652, <https://doi.org/10.1016/j.intermet.2019.106652>.
- [41] H. Kang, K. Song, L. Li, X. Liu, Y. Jia, G. Wang, Y. Wang, S. Lan, X. Lin, L.-C. Zhang, C. Cao, Simultaneously healing cracks and strengthening additively manufactured Co34Cr32Ni27Al4Ti3 high-entropy alloy by utilizing Fe-based metallic glasses as a glue, *J. Mater. Sci. Technol.* 179 (2024) 125–137, <https://doi.org/10.1016/j.jmst.2023.08.048>.
- [42] Z. Yang, J. Bao, C. Ding, S. Son, Z. Ning, J. Xu, D. Shan, B. Guo, H.S. Kim, Electroplasticity in the Al0.6CoCrFeNiMn high entropy alloy subjected to electrically-assisted uniaxial tension, *J. Mater. Sci. Technol.* 148 (2023) 209–221, <https://doi.org/10.1016/j.jmst.2022.11.031>.
- [43] Y. Hao, W. Meng, J. Guan, X. Yao, L. Li, Specific application method for determining the strength and fracture toughness of metal materials, *Theor. Appl. Fract. Mech.* 124 (2023) 103822, <https://doi.org/10.1016/j.tafmec.2023.103822>.
- [44] Z. Lei, P. Gao, H. Li, Y. Cai, M. Zhan, On the fracture behavior and toughness of TA15 titanium alloy with tri-modal microstructure, *Mater. Sci. Eng. A* 753 (2019) 238–246, <https://doi.org/10.1016/j.msea.2019.03.031>.
- [45] S. Li, S. Li, L. Liu, L. Gao, Y. Fu, X. Zhang, B. Li, High temperature softening mechanism of powder metallurgy TA15 alloy, *Mater. Sci. Eng. A* 877 (2023) 145160, <https://doi.org/10.1016/j.msea.2023.145160>.